





Alignment dependence of photoelectron angular distributions in the few-photon ionization of molecules by ultraviolet pulses

Huynh Van Sa Lam , Tomthin Nganba Wangjam , and Vinod Kumarappan ^{*}
James R. Macdonald Laboratory, Kansas State University, Manhattan, Kansas 66506, USA

 (Received 17 February 2022; accepted 22 March 2022; published 11 May 2022)

We probe the time-dependent ionization dynamics of impulsively excited rotational wave packets of N_2 , CO_2 , and C_2H_4 using broadband ultraviolet pulses centered at 262 nm. Photoelectron momentum distributions recorded by velocity-map imaging show a strong dependence on alignment, on multiphoton order, and on the electronic and vibrational states of the cation. We show that substantial information about the molecular-frame photoelectron angular distribution can be obtained from the high-order laboratory-frame asymmetry parameters without any prior knowledge of the photoionization process. We also compare few-photon ionization with one-photon ionization and strong-field ionization.

DOI: [10.1103/PhysRevA.105.053109](https://doi.org/10.1103/PhysRevA.105.053109)

I. INTRODUCTION

Photoelectron spectroscopy has long been an important method to study atomic and molecular structure and dynamics. With advances in ultrafast light sources in a wide range of wavelengths, time-resolved photoelectron energy and angular momentum measurements have become an essential tool for probing chemical transformations in real time [1–10]. Photoelectron-photoion coincidence measurements and molecular alignment techniques have also enabled these measurements to be made in the molecular frame, which provides access to the symmetries of electronic states involved [11–19]. Following a theoretical framework built for single-photon ionization [20–25], Marceau *et al.* have shown that “complete” measurements—wherein the phases and magnitudes of all the relevant photoionization matrix elements are determined—of single-photon ionization of linear molecules is possible with the use of impulsively excited rotational wave packets [26]. The development of such techniques for larger classes of molecules and photoionization processes will enhance the power of photoelectron spectroscopy as a tool for a detailed understanding of molecular dynamics.

In this work, we report the time-dependent few-photon ionization of impulsively excited rotational wave packets of molecules (N_2 , CO_2 , C_2H_4) by broadband ultraviolet (UV) pulses (≈ 262 nm). Without a theoretical framework in the few-photon ionization regime akin to the one used by Marceau *et al.* [26] for single-photon ionization, extracting all the ionization dynamical parameters is beyond the scope of this paper. However, we show that it is possible to independently determine the time-dependent molecular axis distributions and separate their averaging effects from the laboratory-frame photoelectron angular distribution (LFPAD) even without a detailed understanding of the ionization process. This allows

us to simultaneously retrieve angle-dependent ionization rates and partial molecular-orientation-dependent photoionization differential cross sections that are closely related to molecular-frame photoelectron angular distributions (MFPADs). We also found that few-photon ionization shares many interesting similarities with one-photon and strong-field ionization (SFI). We hope our results will motivate more theoretical work on few-photon ionization to complete our picture of ionization processes.

II. METHODS

A. Experimental setup

The experimental setup has been reported elsewhere [27], and only the salient details are mentioned here. Briefly, the output of a Ti:sapphire laser (2 mJ/pulse, 785-nm center wavelength, 35-fs pulse duration, 1-kHz repetition rate) is split by a broadband 40% reflection beam splitter. The reflected pulse is stretched by SF-11 glass, down-collimated by a telescope, and used to align the molecules. In this work, the transmitted pulse is used to generate the third harmonic (≈ 262 nm, ≈ 190 fs) via double- and sum-frequency mixing stages in β -BBO (beta barium borate) crystals, and the third harmonic then serves as the ionizing probe. The delay between the aligning pulse and the probe pulse is varied using a computer-controlled translation stage. Both pulses are linearly polarized parallel to the detector plane. The beams are focused inside a vacuum chamber by a 20-cm-focal-length concave mirror coated for both wavelengths. The laser pulses interact with rotationally cold molecules (< 10 K) produced by supersonic expansion (0.5%–2.0% target gas in He at a total pressure of 70 bars) through an Even-Lavie valve [28].

The LFPADs are recorded by using a velocity map imaging (VMI) spectrometer [29]. By utilizing the synchronization of a mechanical chopper (250 Hz) in the pump beam, the pulsed Even-Lavie valve (500 Hz), and the laser pulses (1 kHz) at different frequencies together with a fast cam-

^{*}vinod@phys.ksu.edu

era (1000 frames/s) and a fast centroiding algorithm, we measure hit-by-hit single-shot data of four different types: pump-probe-gas, pump-probe-no gas, probe-gas, and probe-no gas. Because the scattered UV light causes a background signal (light and electrons) which can affect the analysis, we subtract the background image (pump on, probe on, but no gas) at each delay from the signal image (pump on, probe on, gas on). More details are provided in Appendix A. This step introduces negative values in the low-count area of the image; however, the negative value is typically at the level of a few percent compared to the electron signals from the ionization channels. The corrected two-dimensional (2D) VMI image $M_{2D}(\vec{k}_{2D}, t)$ used in further analysis is

$$M_{2D}(\vec{k}_{2D}, t) = \frac{[\text{pump, probe, gas}] - [\text{pump, probe}]}{\text{yield}[\text{probe, gas}] - \text{yield}[\text{probe}]}, \quad (1)$$

where \vec{k}_{2D} is the projected momentum of the electron on the detector plane, [pump, probe, gas] and [pump, probe] are 2D VMI images, and yield[probe, gas] and yield[probe] are the total yields of the electrons corresponding to different configurations of pump, probe, and gas. To correct for both short- and long-term fluctuations in the gas density and averages over any drifts in the pump-probe overlap, delay scans are repeated multiple times and averaged.

B. Data analysis

In this paper, our approach is similar to the one used by Lam *et al.* [27] for photoion momentum distributions. We would like to determine the alignment-resolved LFPAD (AR-LFPAD), which is the photoionization differential cross section (DCS) that depends on both the photoelectron energy and the orientation of the molecule in the laser field. This AR-LFPAD is denoted by $d\sigma/d\theta d\theta_k dk$, where σ is the photoionization cross section, k is the magnitude of the electron momentum, θ_k is the polar angle between the laser polarization axis and the electron momentum, and θ is the polar angle between the laser polarization axis and the molecular axis (see Fig. 1). Note that the axial symmetry of the measurement about the laser polarization axis precludes the determination of the dependence on azimuthal angles. The AR-LFPAD can be expressed as a linear combination in the basis of the product of two Legendre polynomials $P_J(\cos\theta)P_L(\cos\theta_k)$ for the angular dependence,

$$\frac{d\sigma}{d\theta d\theta_k dk} = \sum_{JL} A_{JL}(k) P_J(\cos\theta) P_L(\cos\theta_k). \quad (2)$$

The AR-LFPAD can be normalized to the alignment-resolved photoelectron spectrum (AR-PES) [30] $R(k, \theta)$ to highlight the distribution of electrons at each molecular orientation. We call it the yield-corrected AR-LFPAD (YCAR-LFPAD):

$$S(\theta, k, \theta_k) = \frac{1}{R(k, \theta)} \frac{d\sigma}{d\theta d\theta_k dk}, \quad (3)$$

where $R(k, \theta)$ can be obtained either by integrating the AR-LFPAD in Eq. (2) over θ_k ,

$$R(k, \theta) = \frac{d\sigma}{d\theta dk} = \int \frac{d\sigma}{d\theta d\theta_k dk} \sin\theta_k d\theta_k, \quad (4)$$

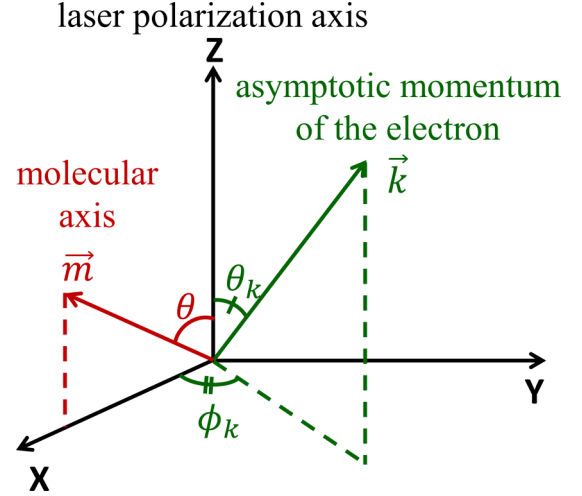


FIG. 1. All angles are defined in the LF, where the Z axis is the laser polarization axis and X is the laser propagation direction. The molecular axis is described by the polar angle θ and the azimuthal angle ϕ . The asymptotic photoelectron momentum is described by the polar angle θ_k , the azimuthal angle ϕ_k , and the magnitude k of the momentum. The angle ϕ is not physically relevant, and the relevant angle $\phi_k - \phi$ is lost because of the axial symmetry of the measurement, so the molecular axis is shown here at an arbitrarily chosen angle $\phi = 0^\circ$. We would like to determine the AR-LFPAD, $d\sigma/d\theta d\theta_k dk$, which is the photoionization DCS that depends on both the photoelectron energy and the orientation of the molecule in the laser field. This AR-LFPAD is closely related to the MFPAD, as discussed in the text.

or by applying linear-regression fitting to the delay-dependent yield of the corresponding channel as shown in Refs. [27,31–35]. We check both methods for consistency. For each particular energy (determined by the momentum k), $R(k, \theta)$ can also be interpreted as the likelihood of ionization as a function of θ .

As discussed in Refs. [20,22,23,25,26], in the laboratory frame (LF), the time-resolved LFPAD $d\sigma(t)/d\theta_k dk$ can be written as a sum of the AR-LFPAD $d\sigma/d\theta d\theta_k dk$ weighted by the delay-dependent molecular axis distribution $\rho(\theta, t)$, illustrating the averaging effect on the observed LFPADs,

$$\frac{d\sigma(t)}{d\theta_k dk} = 2\pi \int \rho(\theta, t) \frac{d\sigma}{d\theta d\theta_k dk} \sin\theta d\theta, \quad (5)$$

or, equivalently,

$$\frac{d\sigma(t)}{d\theta_k dk} = 2\pi \sum_L \left[\sum_J A_{JL}(k) \langle P_J(\cos\theta) \rangle(t) \right] P_L(\cos\theta_k), \quad (6)$$

where the AR-LFPAD was replaced by the expansion in Eq. (2). A more detailed discussion of these equations are provided in Appendix B [see Eqs. (B10) and (B11)].

The three-dimensional (3D) LFPAD at each delay $d\sigma(t)/d\theta_k dk$ can be reconstructed from the VMI data by applying an Abel inversion using the polar basis expansion (pBasex) method [36] due to the axial symmetry of the momentum distribution,

$$\frac{d\sigma(t)}{d\theta_k dk} = 2\pi \sum_L C_L(k, t) P_L(\cos\theta_k), \quad (7)$$

where

$$C_L(k, t) = \sum_{k_0} C_{k_0L}(t) e^{-\frac{(k-k_0)^2}{2\sigma_b^2}}, \quad (8)$$

k_0 and σ_b are the centers and the width of the radial Gaussian functions, and $C_{k_0L}(t)$ is a set of delay-dependent coefficients obtained via pBasex.

By comparing Eqs. (6) and (7), we have the relation between the delay-dependent coefficients $C_L(k, t)$ and the coefficients $A_{JL}(k)$ needed to determine the AR-LFPAD:

$$C_L(k, t) = \sum_J A_{JL}(k) \langle P_J(\cos \theta) \rangle(t). \quad (9)$$

This equation can be solved by using a linear-regression algorithm, called orientation resolution through rotational coherence spectroscopy (ORRCS), as discussed in Refs. [27,31,32,37]. A brief discussion of the ORRCS method follows.

We calculate $\langle P_J(\cos \theta) \rangle(t)$ by solving the time-dependent Schrödinger equation (TDSE) for rigid rotors. By fitting the calculated $\langle P_J(\cos \theta) \rangle(t)$ to the experimentally obtained delay-dependent coefficients $C_L(k, t)$, the coefficients $A_{JL}(k)$ can be determined. The fit is done over a grid of different pump-laser intensities, pulse durations, and gas rotational temperatures near the measured values to ensure the accuracy of these calibrations. The main result is that we can simultaneously determine all three quantities: the AR-LFPAD $S(\theta, k, \theta_k)$, the AR-PES $R(k, \theta)$, and the rotational wave packet $\rho(\theta, t)$. $S(\theta, k, \theta_k)$ and $R(k, \theta)$ are determined through $A_{JL}(k)$ by using Eqs. (2) and (4), while $\rho(\theta, t)$ is determined by the best-fit estimations of the pump-laser fluence and the rotational temperature of the gas and TDSE calculation of the rotational wave packet using these parameters. The averaging over the axis-distribution moments is incoherent [20,22,23,25,26], so polar plots of the angle-dependent ionization rates throughout this paper are physical. The experimental uncertainty is propagated through each step of the data analysis assuming no covariance between quantities (details can be found in Appendix A).

The asymmetry parameters [38] β_L can be written in terms of the C_L coefficients as

$$\beta_L(k, t) = \frac{C_L(k, t)}{C_0(k, t)}, \quad (10)$$

and the angle-integrated cross section is $\sigma(k, t) = 8\pi^2 C_0(k, t)$. In practice, we need to integrate over the finite range (radial width) of the radial momentum k that each channel spans.

In general, the fully resolved LFPAD (FR-LFPAD) can be written as

$$\frac{d\sigma}{dkd\Omega d\Omega_k} = |\langle \psi^e \psi^{\text{ion}} | \hat{\mathbf{O}} | \psi^i \rangle|^2, \quad (11)$$

where ψ^i is the initial state of the molecule, ψ^e is the final state of the photoelectron, ψ^{ion} is the state of the corresponding ion, and $\hat{\mathbf{O}}$ is the light-induced coupling between the initial and final states of the wave function (for example, in one-photon ionization, it is the dipole). $d\Omega$ expresses the dependence on θ and ϕ , and $d\Omega_k$ expresses the dependence

on θ_k and ϕ_k . This FR-LFPAD is equivalent to the MFPAD [or the molecular-frame (MF) interferogram]. Both contain the same information since no averaging has been done, and rotation does not affect the shape of the distribution. They can be transformed into one another by a rotation connecting the two frames.

To fully characterize the photoionization dynamics and fully describe the MFPAD (i.e., perform a “complete” experiment), one needs to determine the magnitudes and phases of all the involved matrix elements [39]. It has been theoretically [22] and experimentally [26] demonstrated that, in the case of one-photon ionization by linearly polarized light of a linear molecule, a measurement with cylindrical symmetry provides enough information to do so, but there is no framework for other cases. Hence, we focus on obtaining best-fit estimates for $A_{JL}(k)$, which determine the AR-LFPAD. These coefficients carry partial but important information about the photoionization process.

We would like to point out two limitations in the information contained in $A_{JL}(k)$. The first is that the ARLFPAD has no ϕ or ϕ_k dependence, which is lost due to the cylindrical symmetry of the LF measurement [see Appendix B, Eqs. (B10) and (B11)]. The second is that, since we do not identify the relevant matrix elements, the AR-LFPAD is truncated based on the convergence of the fit in Eq. (9) (as discussed in Ref. [27]) rather than on angular momentum constraints. Using this procedure, we are still able to reconstruct the MF interferograms (or MFPADs) as mentioned in Ref. [26] with an average about the laser polarization axis without any prior knowledge of the photoionization process.

III. RESULTS AND DISCUSSIONS

A. Nitrogen

In this experiment, cold nitrogen molecules (N_2 at a rotational temperature ≈ 6 K), from the supersonic expansion of a gas mixture of 2% N_2 in He, are aligned by a pump pulse (≈ 150 fs, 34 TW/cm², 785 nm) and then ionized by a third harmonic pulse at different delays. The intensity of the third harmonic is ≈ 2.5 TW/cm², below the saturation ionization of N_2 [41,42]. Figure 2 shows the raw photoelectron VMI spectra for isotropic, aligned, and antialigned distributions [Figs. 2(a)–2(c)] and the energy-calibrated spectrum [Fig. 2(d)]. By comparing the locations of the peaks seen in Fig. 2(d) with spectroscopic data [40], we can identify photoelectrons ionized into several ionic states with different numbers of photons absorbed, as shown in Fig. 2(d). A strong dependence of the photoelectron angular distributions (PADs) on the alignment, on electronic and vibrational states of the cation, and on photon numbers can be seen already in raw VMI images [Figs. 2(a)–2(c)].

As discussed in Sec. II B, we can reconstruct the delay-dependent 3D LFPADs by applying the pBasex inversion algorithm [36] to the VMI image at each delay. These distributions are described, through Eq. (7), by a set of delay-dependent coefficients $C_L(k, t)$. The modulations of the LFPADs of different channels as the wave packet evolves are depicted more clearly in delay-momentum maps of these coefficients in Fig. 2(e).

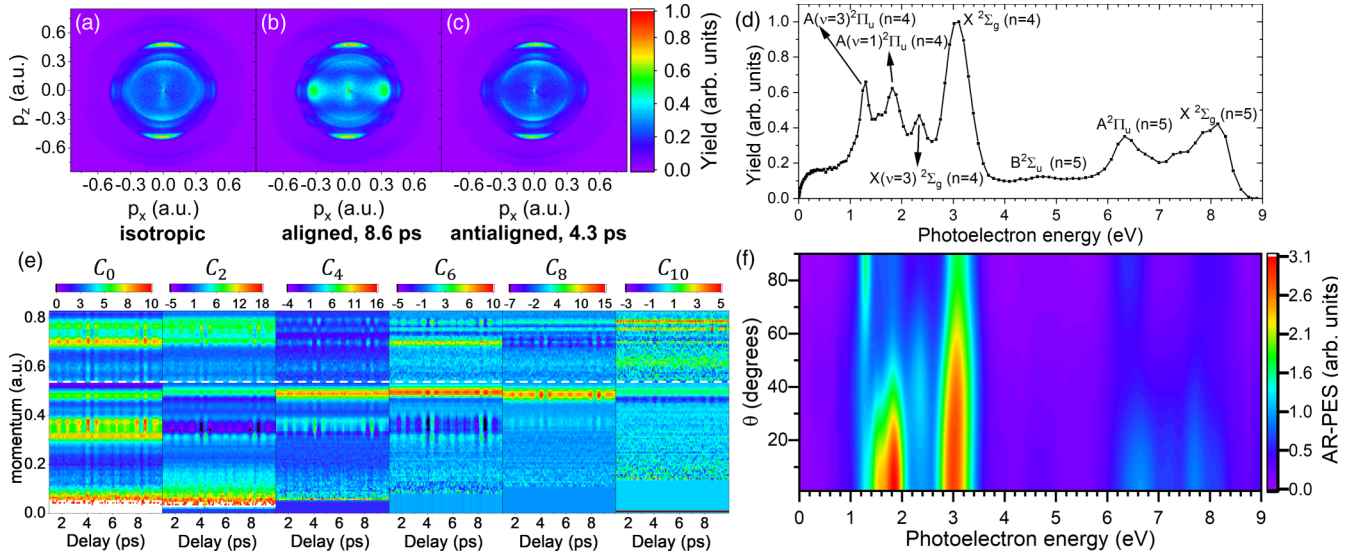


FIG. 2. VMI images of the photoelectron momentum from N_2 at the (a) isotropic, (b) aligned, and (c) antialigned distributions. The laser polarization is along the p_z direction. The linear color scale expresses the yield of the electrons in arbitrary units; the same scale is used in all images. Using the pBasex algorithm [36], the VMI image of the isotropic distribution is converted to energy and angular distributions as shown in (d), with ionic states and photon numbers n identified using spectroscopic data [40]. (e) A delay-momentum map of the pBasex coefficients. These coefficients describe the modulation of the time-resolved LFPAD as a function of the electron asymptotic momentum k and the pump-probe delay t through Eq. (7). Signals for $k > 0.53$ a.u. were multiplied by 10 for clarity. Even these faint channels show clear modulations with time. We implemented the Nyquist theorem by dropping the low- k , high- L basis functions; that is, data near the center of the image (low k) do not have enough resolution to resolve complex angular structure (high L). (f) The AR-PES [see Eq. (4)]. Each vertical line is the angle-dependent ionization rate at a specific photoelectron momentum k describing the ionization yield at different orientations of the molecular axis θ in the laser field.

By applying regression analysis [27] to the delay-dependent yield, we retrieve the relative AR-PES [see Eq. (4)], as shown in Fig. 2(f). Each vertical line is the angle-dependent ionization rate at a specific photoelectron momentum k . The energy-integrated angle-dependent ionization rate has a peanut shape and peaks along the laser polarization axis ($\theta = 0^\circ$). Petretti *et al.* theoretically predicted the wavelength- and alignment-dependent photoionization of N_2 [43] by weighting the angle-dependent contributions of ionization from different orbitals. At 266 nm, the ionization rate of the second-highest occupied molecular orbital (HOMO-1) with π_u symmetry peaks perpendicular to the molecular axis and contributes significantly to the total ionization rate. The discrepancy from our results suggests further considerations are needed, such as the role of the intermediate and excited states, or a different weighting (of the angle-integrated cross section) between channels. Although nitrogen has no valence-excited states that could be dipole excited by a single photon of our UV pulse and only one singlet gerade state ($a^1\Pi_g$) that is accessible by two-photon excitation, there are several singlet ungerade states that can be reached via three-photon excitation [44,45]. Moreover, the duration of the UV pulse (≈ 190 fs) is long enough for significant vibrational motion in these intermediate states, further broadening the possible pathways. The determination of the intermediate resonances that contribute to our four- and five-photon ionization signals is therefore difficult, and we have not tried to do so.

The four-photon ionization to the ground state, $X^2\Sigma_g$, of the ion is presented in Fig. 3. Figure 3(a) shows the average delay-dependent coefficients $C_L(k, t)$ and their corresponding

fits. We observed strong modulation of these coefficients as a function of delay and obtained good fits using linear regression through Eq. (9). With these fits, we retrieved the coefficients $A_{JL}(k)$ and thus determined the angle-dependent ionization rate [Fig. 3(b)] and the YCAR-LFPAD [Fig. 3(c)]. Tables of the $A_{JL}(k)$ coefficients for all channels presented in the paper are provided in Appendix C.

The angle-dependent ionization rate in this case looks similar to the previous result from SFI by Pavičić *et al.* [46] and hence still reflects the σ_g symmetry of the HOMO. In Fig. 3(c), the YCAR-LFPAD $S(\theta, k, \theta_k)$ shows a transition from a three-lobe structure at $\theta \approx 0^\circ$ to a two-lobe structure at $\theta_k \approx 90^\circ$. When the molecule is parallel to the laser polarization direction ($\theta \approx 0^\circ$), the PAD shows three peaks at $\theta_k \approx 0^\circ$ (along the laser polarization axis), $\theta_k \approx 90^\circ$ (perpendicular to the laser polarization axis), and $\theta_k \approx 50^\circ$. When the molecule is perpendicular to the laser polarization direction ($\theta \approx 90^\circ$), the PAD still shows the peaks at $\theta_k \approx 0^\circ$ and $\theta_k \approx 90^\circ$, but the peak at $\theta_k \approx 50^\circ$ that is seen near $\theta = 0^\circ$ has faded away.

Figure 3 also shows a comparison between the LFPAD at peak alignment [Fig. 3(d), dashed line] and antialignment [Fig. 3(e), dashed line] with the YCAR-LFPAD $S(\theta, k, \theta_k)$ at $\theta = 0^\circ$ [Fig. 3(d), solid line] and $\theta = 90^\circ$ [Fig. 3(e), solid line]. The similarity of the DCS at $\theta = 0^\circ$ and the LFPAD at peak alignment suggests that, at this degree of alignment ($(\cos^2 \theta)_{\max} \approx 0.78$), the measurement of LFPADs gets very close to the MFPADs. This can serve as a useful test case to benchmark different methods of constructing the MFPADs. Direct measurements of 3D LFPADs without axial symmetry

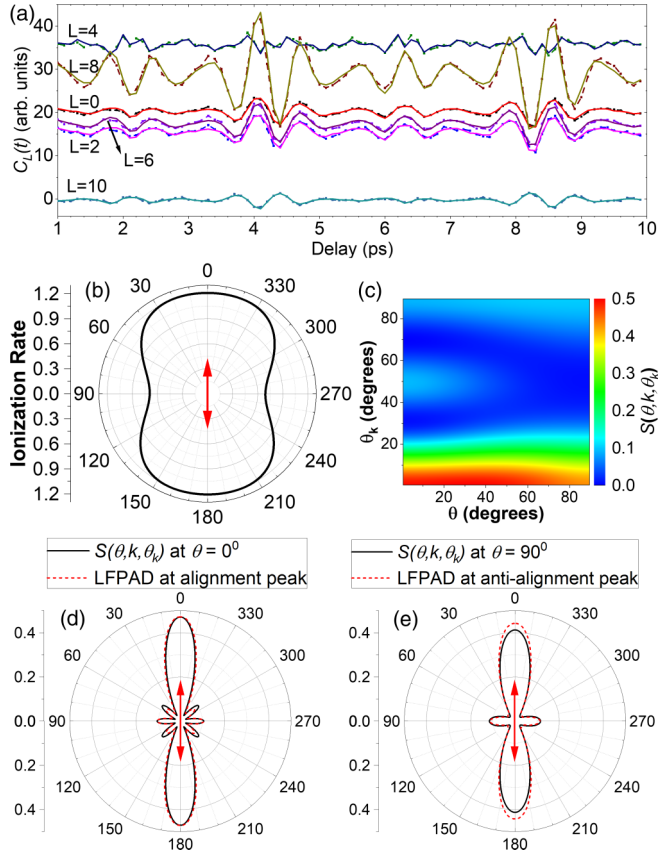


FIG. 3. Results for ionization of N_2 into the $X^2\Sigma_g(n=4)$ ionic state (k is integrated from 0.44 to 0.53 a.u.): (a) The delay-dependent pBasex coefficients $C_L(t)$ (dashed lines with squares) and their corresponding fits (solid lines) as described in Eq. (9). From these fits, we can retrieve (b) the angle-dependent ionization rate and (c) the YCAR-LFPAD $S(\theta, k, \theta_k)$ as in Eq. (3). The angle-dependent ionization rate looks similar to the previous result from SFI [46]. We compare the vertical slice of $S(\theta, k, \theta_k)$ at $\theta = 0^\circ$ with the LFPAD at the alignment peak in (d), and the slice of $S(\theta, k, \theta_k)$ at $\theta = 90^\circ$ with the LFPAD at the anti-alignment peak in (e). The angle in the polar plots in (d) and (e) is θ_k . Their similarities indicate these measurements in the LF are a good representation of the MF. The laser polarization axis is indicated by the red arrow.

using the tomographic imaging technique [47–49] would then be a useful comparison, although the simultaneous rotation of the polarization axes of two different wavelengths can be a challenge.

Similar results for four-photon ionization into three vibrational levels ($\nu = 1-3$) of the first excited state of the ion, $A^2\Pi_u$, are presented in Fig. 4. In comparison with ionization into the ground state, $X^2\Sigma_g(n=4)$, the angle-dependent ionization rates show a significant contribution from the perpendicular orientation that was not observed in Fig. 3(b). The ionization rates become more isotropic for higher vibrational levels. Different behaviors of these vibrational levels also suggest that they go through different intermediate states before ionization.

In general, the diagonal trend in the YCAR-LFPAD shows that electrons from ionization to the first excited state of the ion, $A^2\Pi_u$, are distributed mainly perpendicular to the

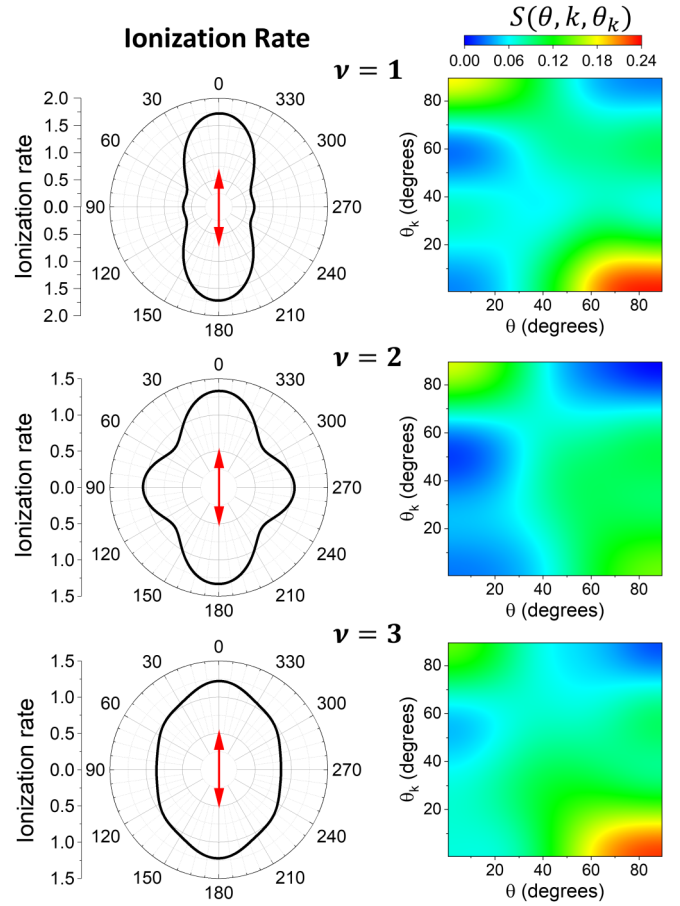


FIG. 4. Results for ionization of N_2 into three different vibrational levels of the first excited state $A^2\Pi_u(n=4)$ of the cation. Left: The angle-dependent ionization rate. Right: The YCAR-LFPAD $S(\theta, k, \theta_k)$. All three 2D plots use the same color scale shown at the top. Different vibrational levels are $\nu = 1-3$ from top to bottom. The momentum k is integrated in the ranges of 0.267–0.316 a.u. for $\nu = 1$, 0.316–0.337 a.u. for $\nu = 2$, and 0.344–0.387 a.u. for $\nu = 3$.

molecular axis ($\theta_k \approx 90^\circ - \theta$), which may be connected to the π_u symmetry of the HOMO-1 orbital. This signature was not reflected clearly in the ionization rates. This strong dependence on the molecular orientation is completely different from the distribution of electrons ionized into the ground state, $X^2\Sigma_g(n=4)$.

B. Carbon dioxide

In the case of carbon dioxide (CO_2), cold molecules (≈ 4 K), from the supersonic expansion of a gas mixture of 0.5% CO_2 in He, are aligned with a pump pulse (≈ 150 fs, 13 TW/cm², 785 nm) and then ionized by a third harmonic pulse (≈ 2 TW/cm², below the saturation ionization of CO_2 [42]).

We observed a dominant channel at electron energy ≈ 0.4 eV, corresponding to three-photon ionization into the ground state, $X^2\Pi_g$, of the cation. Raw VMI images in Figs. 5(a) and 5(b) already show distinguishable features in directions parallel and perpendicular to the laser polarization axis. The delay-dependent coefficients $C_L(k, t)$ and their corresponding fits are shown in Fig. 5(c). We obtained strong

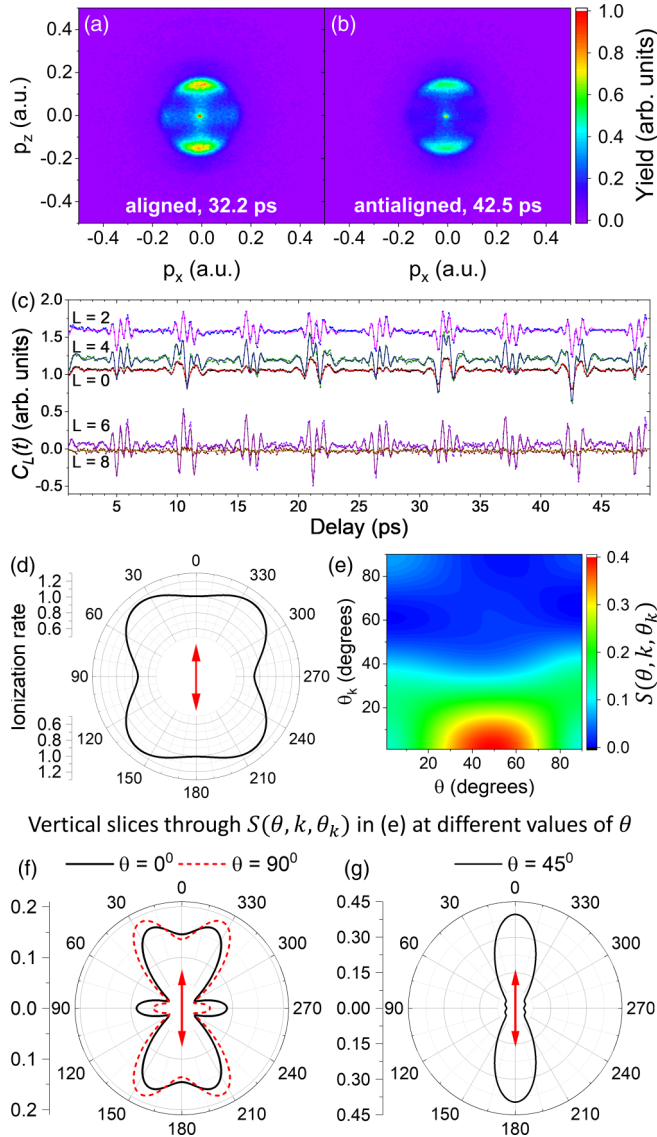


FIG. 5. Three-photon ionization of CO_2 into the ground state, $\tilde{X}^2\Pi_g$, of the ion. Top: VMI electron images at the (a) alignment and (b) antialignment peaks. (c) The delay-dependent coefficients $C_L(k, t)$ and their corresponding fits. The range of k averaged is from 0.12 to 0.19 a.u. (d) The angle-dependent ionization rate. (e) The YCAR-LFPAD. Bottom: Slices of the YCAR-LFPAD (f) at $\theta = 0^\circ$ and 90° and (g) at 45° . The laser polarization axis is indicated by the red arrow.

modulations and good fits up to $L = 6$, while higher-order coefficients are much smaller.

Here, the angle-dependent ionization rate in Fig. 5(d) still has a butterfly shape, similar to the previous results from SFI [27,50], although the dip at 0° is less pronounced. The angle-resolved YCAR-LFPAD $S(\theta, k, \theta_k)$ in Fig. 5(e) is also fairly symmetric about $\theta \approx 45^\circ$. Three slices of the YCAR-LFPAD at $\theta = 0^\circ$, 45° , and 90° are presented in Figs. 5(f) and 5(g). Slices at $\theta = 0^\circ$ and 90° have a butterfly shape together with a peak perpendicular to the laser polarization axis ($\theta_k = 90^\circ$), while the slice at $\theta = 45^\circ$ has a peanut shape with no feature at

($\theta_k = 90^\circ$). All these observed features suggest that the PADs still reflect the π symmetry of the HOMO.

C. Ethylene

The analysis that we presented is general and can be extended to different types of molecule and laser polarizations. For asymmetric top molecules, both Euler angles, θ and χ , are needed to describe the relative orientation between the molecule and a linearly polarized laser field [31] (in the MF, the Euler angles θ and χ are the polar and azimuthal angles describing the laser polarization vector). In practice, however, the YCAR-LFPAD reconstruction requires a much larger set of expansion coefficients $A_{JKL}(k)$ to be determined and a more sophisticated interpretation [51]. In this paper, we limit our discussion to the AR-PES (or the molecular-frame angle- and energy-dependent ionization rate) $R(k, \theta, \chi)$. Unlike in [31], where the ions were measured to deduce $R(k, \theta, \chi)$ for SFI, in few-photon ionization and by using the VMI technique, we can separately determine $R(k, \theta, \chi)$ for multiple channels with electrons corresponding to different states of the cations.

A measurement was made on ethylene (C_2H_4) where rotationally cold molecules (≈ 4 K), from the supersonic expansion of a gas mixture of 0.5% target gas in He, are aligned with a pump pulse (≈ 200 fs, 4 TW/cm², 785 nm) and then ionized by a third harmonic pulse (≈ 2 TW/cm²). The photoelectron spectrum shows two distinct channels, with the electron energies ≈ 3.7 eV and ≈ 1.4 eV, corresponding to three-photon ionization into the ground state, \tilde{X}^2B_{3u} , and the first excited state, \tilde{A}^2B_{3g} , of the ion as shown in Figs. 6(a) and 6(b). By fitting to the delay-dependent yields of these two channels using linear regression in Fig. 6(c), we can retrieve the full molecular-frame angle-dependent ionization rates $R(\theta, \chi)$ that depend on both Euler angles for each channel [27,31,32], as shown in Figs. 6(d) and 6(e).

The results share many similarities with previous measurements in the SFI regime [31]. The ionization probability in the ground state, \tilde{X}^2B_{3u} , has a maximum at $\theta = 90^\circ$ and $\chi = 90^\circ$. This is similar to the angle-dependent probability of the nondissociative strong-field ionization obtained by measuring the C_2H_4^+ ion, which was assigned to the removal of an electron from the HOMO [31]. On the other hand, the ionization into the first excited state, \tilde{A}^2B_{3g} , prefers molecules aligned near $\theta = 45^\circ$ and $\chi = 0^\circ$. This is similar to the angle-dependent probability of the dissociative ionization in the strong field obtained by measuring the C_2H_3^+ and C_2H_2^+ ions, which was previously assigned to removing a HOMO-1 electron [31].

IV. CONCLUSIONS

We investigated the time-dependent ionization dynamics of impulsively excited rotational wave packets of molecules using broadband UV pulses for ionization and fundamental 785-nm pulses for alignment. The PADs show a strong dependence on alignment, on multiphoton order, and on electronic and vibrational states, indicating that these PADs are sensitive to molecular structure and dynamics.

We have shown that, without prior knowledge of the photoionization process, partial but substantial information about

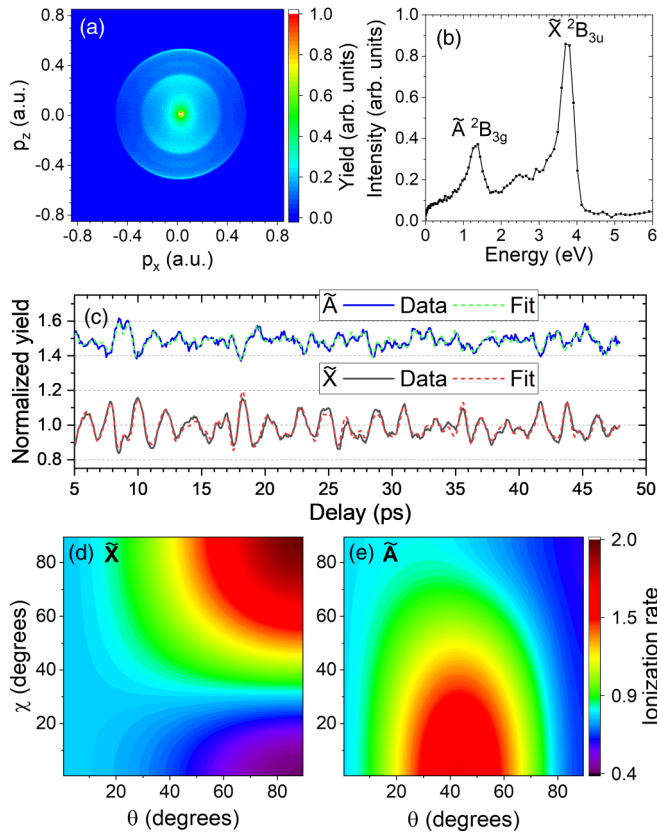


FIG. 6. Results on three-photon ionization of C_2H_4 into the ground state, \tilde{X}^2B_{3u} , and the first excited state, \tilde{A}^2B_{3g} , of the ion. Top: (a) An example of a VMI electron image and (b) the calibrated energy with ionic states identified by using spectroscopic data [52]. (c) The delay-dependent electron yields of the two channels and their corresponding fits. The first excited state, \tilde{A}^2B_{3g} , was shifted up by 0.5 for clarity. Bottom: The angle-dependent ionization rates $R(\theta, \chi)$ of (d) the ground state and (e) the excited state. The momentum k is integrated in the ranges of 0.22–0.34 a.u. for the \tilde{X}^2B_{3u} state and 0.46–0.54 a.u. for \tilde{A}^2B_{3g} .

the MFPAD (with an average about the laser polarization axis) can still be retrieved from the highly anisotropic laboratory-frame data using a fitting algorithm. This partial MFPAD, or a large set of extracted coefficients describing it, can be compared with theory to better understand multiphoton ionization of molecules. The determination of a full MFPAD, together with complex matrix elements describing the electronic coherences and ionization dynamics, requires further developments of a proper ionization model and a complex theoretical framework, especially for different types of molecules and polarization geometries. A better understanding of the MFPAD is necessary since time-resolved MFPAD is a promising probe of molecular dynamical processes.

Few-photon ionization is in the middle regime between the better-understood one-photon ionization and SFI. In many cases, we found similarities between the angle-dependent ionization rates from few-photon ionization and from a strong field. In SFI, the widely used MO-ADK model connects the angle-dependent ionization rate to the shape and the symmetry of the molecular orbitals [53]; however, such connection has

not been established in the few-photon ionization regime. In a one-photon process, the transition is either parallel or perpendicular, and the angle dependence of the ionization rate can be only either $\cos^2\theta$ or $\sin^2\theta$ since the ionization yield depends on only the second-order moment of the molecular axis distribution. n -photon ionization allows resolution up to the $2n^{\text{th}}$ -order moment [25], which can reveal more details if one can decode the relationship between the angle-dependent ionization rate and the molecular states. On the other hand, the PADs in few-photon ionization are very sensitive to molecular structure and dynamics, which is similar to one-photon ionization, while electrons in a strong field are typically distributed along the laser polarization and are less sensitive to the molecular dynamics. More investigations of the few-photon ionization regime are needed to complete our picture of ionization processes and to gain the advantages of the knowledge we obtained from the other two regimes.

ACKNOWLEDGMENT

This work was supported by the U.S. Department of Energy, Office of Science, Basic Energy Sciences, under Award No. DE-FG02-86ER13491.

APPENDIX A: PROPAGATION OF UNCERTAINTY AND NORMALIZATION

Assuming there is no covariance between quantities, the uncertainty of simple functions of the real variables A and B , with standard deviations σ_A and σ_B and exactly known (deterministic) real-valued constants a and b , can be propagated using the following formulas:

Function	Standard deviation
$f = aA$	$ a \sigma_A$
$f = aA \pm bB$	$\sqrt{a^2\sigma_A^2 + b^2\sigma_B^2}$
$f = AB$ or A/B	$ f \sqrt{(\sigma_A/A)^2 + (\sigma_B/B)^2}$

In the first step, after constructing the corrected time-dependent VMI images as described in Eq. (1), we then estimate the uncertainty of the mean of each pixel (i, j) at each delay by the statistical error

$$\sigma_m(i, j) = \frac{\sigma_d(i, j)}{\sqrt{N}}, \quad (\text{A1})$$

where σ_d is the width of the distribution and N is the number of scans. For each VMI image, we have a corresponding image of uncertainty with pixel-to-pixel mapping.

Since the VMI images are fourfold symmetric, we can fold each image into one quadrant to increase the statistics. At this step, the uncertainties of the four averaged pixels are added in quadrature. The images can also be Gauss smoothed to reduce pixel noise. Since convolution with a Gaussian filter generated a weighted average of neighboring pixels, the uncertainty can be calculated by using the expression for $f = aA + bB$ from the table. Both the error image and the Gaussian kernel are squared element by element and then convoluted. The square

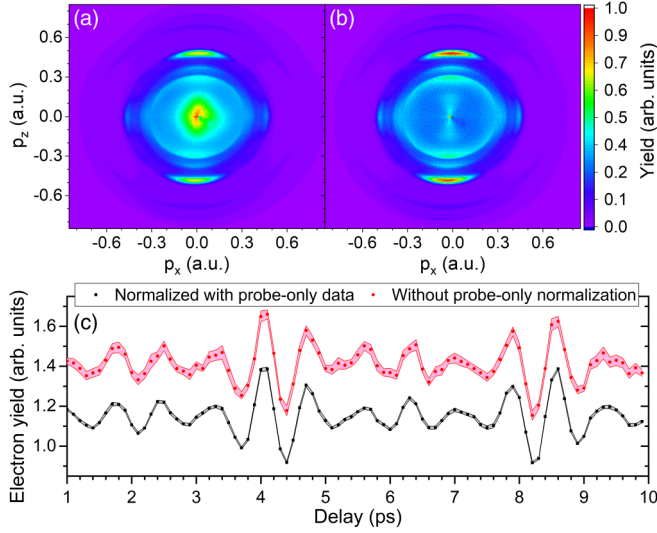


FIG. 7. (a) Electron image with [probe, gas]. (b) Electron image with [probe, background] subtracted from [probe, gas]. (c) Delay-dependent electron yield with and without probe-alone normalization. The red curve has been normalized to its mean and shifted up by 0.25. See text for more details.

root of the result then gives the new error estimate for the VMI image.

These VMI images and their corresponding uncertainty images are then fed into the pBasex algorithm for inversion. The original pBasex algorithm [36] does not treat uncertainty and does not produce the uncertainty of the output coefficients. Our version of pBasex weights the mean value of each pixel with its uncertainty and uses linear regression through singular-value decomposition to find the fitting coefficients $C_L(k, t)$ and their errors. Like in the previous steps, errors were propagated through Eq. (8). For each channel, we average over a range of radial momentum k ; we then obtain the average delay-dependent coefficients and their uncertainty for the channel, $C_{kL}(t) \pm \sigma_{kL}^C(t)$.

Finally, these delay-dependent coefficients and errors are fed into the ORRCS algorithm that uses linear regression to retrieve the real coefficients, $A_{JL}(k) \pm \sigma_{JL}^A(k)$, which determine the YCAR-LFPAD through Eq. (3).

In Fig. 7, we illustrate the effect of data normalization described in Sec. II A. Figure 7(a) is [probe, gas], and Fig. 7(b) is [probe, gas] with [probe, background] subtracted. The scattered background appears near the center of the image. This scattered background influences the inversion since lower-energy signals will be counted partly as a contribution from higher-energy channels. In Fig. 7(c), we show that the normalization with probe-only data improves the signal-to-noise ratio by correcting gas density and laser intensity fluctuation. The black curve with squares is

$$\frac{Y[\text{pump, probe, gas}] - Y[\text{pump, probe}]}{Y[\text{probe, gas}] - Y[\text{probe}]}.$$
 (A2)

The red curve with circles is

$$Y[\text{pump, probe, gas}] - Y[\text{pump, probe}].$$
 (A3)

We can see that the normalized data are smoother with a much smaller error bar compared to those without normalization. This is for the first 20 scans. We completed 80 scans in total, so the actual error bar should be about 2 times smaller. This correction becomes more important for higher-order coefficients and polyatomic molecules where the modulation of the signal is weaker.

APPENDIX B: MATH ON COMPLEX AMPLITUDES

In this Appendix, we describe the connection between the full MFPAD and the partial MFPAD that we have retrieved in this paper. We will explain why the information about the laser polarization direction was lost because of the cylindrical symmetry of the LF measurement and what needs to be done to recover this dependence and spell out the relation between our retrieved real coefficients and the complex coefficients that describe the outgoing photoelectron wave function.

In the LF, consider a molecule at an orientation described by $(\theta, \phi = 0)$; it is ionized by a linearly polarized pulse. The outgoing photoelectron wave function, in its asymptotic form, can be written as

$$\psi^e = \frac{e^{ikr}}{r} \sum_{lm} \tilde{c}_{lm}(\theta, k) Y_l^m(\theta_k, \phi_k),$$
 (B1)

where all the molecular and ionization dynamics are encoded in the $\tilde{c}_{lm}(\theta, k)$ coefficients.

The wave function for a molecule at any orientation described by an arbitrary azimuthal angle ϕ and the same polar angle θ can be obtained by rotating this function about the LF Z axis.

$$\begin{aligned} \psi^e &= \frac{e^{ikr}}{r} \sum_{lm} \tilde{c}_{lm}(\theta, k) \\ &\times \sum_{m'} D_{m'm}^J(\phi, \theta = 0, \chi = 0) Y_l^{m'}(\theta_k, \phi_k), \end{aligned}$$
 (B2)

where \tilde{c}_{lm} is outside of the m' summation since it does not depend on ϕ .

In this case, the Wigner D rotation matrix reduces to

$$D_{m'm}^J(\phi, \theta = 0, \chi = 0) = \sum_{m'} e^{-im'\phi} \delta_{mm'}.$$
 (B3)

Hence, the wave function is

$$\psi^e = \frac{e^{ikr}}{r} \sum_{lm} \tilde{c}_{lm}(\theta, k) e^{-im\phi} Y_l^m(\theta_k, \phi_k).$$
 (B4)

This form of the equation shows that only the difference between ϕ and ϕ_k (i.e., $\phi - \phi_k$) matters and not the absolute values of the two angles because $Y_l^m(\theta_k, \phi_k) \sim e^{im\phi_k}$.

In scattering theory, the outgoing wave is written in the form of $\frac{e^{ikr}}{r} f(\theta_k, \phi_k)$, and the differential cross section will then be defined as $|f(\theta_k, \phi_k)|^2$. Therefore, the FR-LFPAD that depends on the molecular orientation in this case is

$$\frac{d\sigma}{dkd\Omega d\Omega_k} = \left| \sum_{lm} \tilde{c}_{lm}(\theta, k) e^{-im\phi} Y_l^m(\theta_k, \phi_k) \right|^2,$$
 (B5)

where $d\Omega$ expresses the dependence on θ and ϕ and $d\Omega_k$ expresses the dependence on θ_k and ϕ_k . This FR-LFPAD is equivalent to the MFPAD (or the MF interferogram) written in LF angles (i.e., θ , ϕ , θ_k , ϕ_k). It can be expressed in terms of the MF angles by a rotation connecting the two frames. Both contain the same information since no averaging has been done, and rotation does not affect the shape of the distribution.

The squared modulus in Eq. (B5) can be written as a double sum,

$$\frac{d\sigma}{dkd\Omega d\Omega_k} = \sum_{lm} \sum_{l'm'} \tilde{c}_{lm}(\theta, k) \tilde{c}_{l'm'}^*(\theta, k) e^{-i(m-m')\phi} \times Y_l^m(\theta_k, \phi_k) [Y_{l'}^{m'}(\theta_k, \phi_k)]^*. \quad (\text{B6})$$

This expression can be simplified by expanding the product of the two spherical harmonics as a series by using the contraction rule

$$\frac{d\sigma}{dkd\Omega d\Omega_k} = \sum_{lm} \sum_{l'm'} \tilde{c}_{lm}(\theta, k) \tilde{c}_{l'm'}^*(\theta, k) e^{-i(m-m')\phi} \times \sum_{LM} \langle l, 0, l', 0 | L0 \rangle \langle l, m, l', -m' | LM \rangle \times (-1)^{m'} \sqrt{\frac{(2l+1)(2l'+1)}{4\pi(2L+1)}} Y_L^M(\theta_k, \phi_k). \quad (\text{B7})$$

The dependence of the $\tilde{c}_{lm}(\theta, k)$ coefficients on the polar angle θ can be expanded in the Legendre polynomial basis as

$$\tilde{c}_{lm}(\theta, k) = \sum_j \tilde{a}_{lmj}(k) P_j(\cos \theta). \quad (\text{B8})$$

The FR-LFPAD then becomes

$$\frac{d\sigma}{dkd\Omega d\Omega_k} = \sum_{lm} \sum_{l'm'} \sum_{LM} \sum_{jj'} \tilde{a}_{lmj}(k) \tilde{a}_{l'm'j'}^*(k) \times (-1)^{m'} e^{-i(m-m')\phi} P_j(\cos \theta) P_{j'}(\cos \theta) \times \langle l, 0, l', 0 | L0 \rangle \langle l, m, l', -m' | LM \rangle \times \sqrt{\frac{(2l+1)(2l'+1)}{4\pi(2L+1)}} Y_L^M(\theta_k, \phi_k). \quad (\text{B9})$$

The product of two Legendre polynomials can also be expanded in a series; this leads to

$$\frac{d\sigma}{dkd\Omega d\Omega_k} = \sum_{lm} \sum_{l'm'} \sum_{LM} \sum_{jj'} \sum_J \tilde{a}_{lmj}(k) \tilde{a}_{l'm'j'}^*(k) \times (-1)^{m'} e^{-i(m-m')\phi} \times \langle j, 0, j', 0 | J0 \rangle^2 P_J(\cos \theta) \times \langle l, 0, l', 0 | L0 \rangle \langle l, m, l', -m' | LM \rangle \times \sqrt{\frac{(2l+1)(2l'+1)}{4\pi(2L+1)}} Y_L^M(\theta_k, \phi_k). \quad (\text{B10})$$

As discussed in Refs. [20,23,25,26], the measured LFPAD is a summation of the FR-LFPAD in Eq. (B10) weighted by the time-dependent molecular axis distribution $\rho(\theta, t)$ excited

by the alignment pulse. Technically, we need to multiply Eq. (B10) by $\rho(\theta, t)$ and average over θ and ϕ .

Since $\rho(\theta, t)$ does not depend on ϕ , we can perform the integration over ϕ independently first, then multiply by $\rho(\theta, t)$ and average over θ later. The integral over ϕ is nonzero only if $m = m'$, which makes $M = 0$. This gives

$$\frac{d\sigma}{dkd\theta d\theta_k} = 2\pi \sum_L \sum_J \sum_{l'l'm} \sum_{jj'} \tilde{a}_{lmj}(k) \tilde{a}_{l'm'j'}^*(k) \times \frac{(-1)^m}{4\pi} \sqrt{(2l+1)(2l'+1)} \times \langle j, 0, j', 0 | J0 \rangle^2 \times \langle l, 0, l', 0 | L0 \rangle \langle l, m, l', -m | L0 \rangle \times P_J(\cos \theta) P_L(\cos \theta_k), \quad (\text{B11})$$

where the dependence on ϕ and ϕ_k is gone.

The $\rho(\theta, t)$ -weighted integration over θ then gives us the time-dependent photoelectron spectrum measured in the LF,

$$\frac{d\sigma(t)}{dkd\theta_k} = 2\pi \sum_L \sum_J \sum_{l'l'm} \sum_{jj'} \tilde{a}_{lmj}(k) \tilde{a}_{l'm'j'}^*(k) \times \frac{(-1)^m}{4\pi} \sqrt{(2l+1)(2l'+1)} \times \langle j, 0, j', 0 | J0 \rangle^2 \times \langle l, 0, l', 0 | L0 \rangle \langle l, m, l', -m | L0 \rangle \times \langle P_J(\cos \theta)(t) \rangle P_L(\cos \theta_k), \quad (\text{B12})$$

where

$$\langle P_J(\cos \theta) \rangle(t) = \int P_J(\cos \theta) \rho(\theta, t) \sin \theta d\theta \quad (\text{B13})$$

are time-dependent axis distribution moments.

TABLE I. $A_{JK}(k)$ coefficients for four-photon ionization of N_2 into three different vibrational levels of the first excited state $A^2\Pi_u$ of the cation.

L	$J = 0$	$J = 2$	$J = 4$	$J = 6$
$\nu = 1$				
0	6.83 ± 0.01	6.50 ± 0.04	3.01 ± 0.06	-0.25 ± 0.08
2	0.34 ± 0.02	-8.74 ± 0.08	-3.79 ± 0.12	0.67 ± 0.16
4	2.94 ± 0.02	6.98 ± 0.10	5.37 ± 0.16	2.23 ± 0.21
6	1.38 ± 0.02	-10.96 ± 0.12	-7.28 ± 0.19	-4.39 ± 0.25
8	0.51 ± 0.03	2.29 ± 0.14	2.14 ± 0.21	0.69 ± 0.29
$\nu = 2$				
0	3.35 ± 0.01	0.13 ± 0.03	1.17 ± 0.04	0.05 ± 0.06
2	1.33 ± 0.01	-4.36 ± 0.06	-1.13 ± 0.08	-0.60 ± 0.11
4	-0.74 ± 0.01	3.42 ± 0.07	1.80 ± 0.11	1.27 ± 0.15
6	0.47 ± 0.02	-3.00 ± 0.09	-0.15 ± 0.13	-1.1 ± 0.18
8	0.05 ± 0.02	-0.26 ± 0.10	0.41 ± 0.15	0.05 ± 0.20
$\nu = 3$				
0	5.73 ± 0.01	0.05 ± 0.04	0.17 ± 0.06	0.27 ± 0.08
2	4.36 ± 0.02	-4.89 ± 0.08	-2.25 ± 0.12	-0.46 ± 0.16
4	0.76 ± 0.02	0.40 ± 0.11	1.21 ± 0.16	2.84 ± 0.22
6	1.66 ± 0.03	-5.47 ± 0.13	1.80 ± 0.19	-1.73 ± 0.26
8	0.09 ± 0.03	-0.65 ± 0.15	0.14 ± 0.22	0.20 ± 0.30

TABLE II. $A_{JK}(k)$ coefficients for four-photon ionization of N_2 into the $X^2\Sigma_g$ ionic state.

L	$J = 0$	$J = 2$	$J = 4$	$J = 6$
0	15.91 ± 0.01	7.16 ± 0.05	-1.94 ± 0.07	-0.54 ± 0.10
2	11.72 ± 0.02	8.11 ± 0.10	-3.28 ± 0.15	3.08 ± 0.21
4	30.81 ± 0.03	3.90 ± 0.14	-10.21 ± 0.21	-0.24 ± 0.28
6	12.99 ± 0.03	9.53 ± 0.16	-1.10 ± 0.24	-0.39 ± 0.32
8	19.26 ± 0.04	24.91 ± 0.18	2.42 ± 0.27	-2.41 ± 0.37
10	0.50 ± 0.04	-3.05 ± 0.19	-1.25 ± 0.29	1.19 ± 0.39

The expression in Eq. (B12) is equivalent to Eq. (6) in Sec. II B. By comparing the two, we can obtain

$$A_{JL}(k) = \sum_{l'l'm} \sum_{jj'} \tilde{a}_{lmj}(k) \tilde{a}_{l'mj'}^*(k) \times \frac{(-1)^m}{4\pi} \sqrt{(2l+1)(2l'+1)} \times \langle j, 0, j', 0 | J0 \rangle^2 \times \langle l, 0, l', 0 | L0 \rangle \langle l, m, l', -m | L0 \rangle, \quad (\text{B14})$$

where $A_{JL}(k)$ are the real coefficients that we retrieved in the paper.

The complex coefficients $\tilde{a}_{lmj}(k)$, and hence $\tilde{c}_{lm}(k)$ and the outgoing photoelectron wave function, can be retrieved by fitting the real coefficients $A_{JL}(k)$ to the expansion in Eq. (B14). A proper ionization model limits the number of terms involved in the fit. Without constraints imposed by the knowledge of the ionization process, the parameter space is too large, and the fitting problem becomes too big to solve reliably. In other words, it can become a massive underdeterministic problem where the number of parameters that need to be determined is much higher than the number of independent parameters that can be measured in the LF.

TABLE III. $A_{JK}(k)$ coefficients for three-photon ionization of CO_2 into the ground state $\tilde{X}^2\Pi_g$ of the ion.

L	$J = 0$	$J = 2$	$J = 4$	$J = 6$
0	1.00 ± 0.001	0.44 ± 0.003	-0.35 ± 0.006	0.06 ± 0.008
2	1.65 ± 0.001	0.51 ± 0.006	-1.37 ± 0.012	0.04 ± 0.018
4	1.15 ± 0.001	1.03 ± 0.008	-1.47 ± 0.016	-0.08 ± 0.023
6	0.19 ± 0.002	0.48 ± 0.098	-2.04 ± 0.019	-0.41 ± 0.028
8	-0.01 ± 0.002	0.01 ± 0.011	-0.19 ± 0.021	-0.09 ± 0.032

In this paper, we did not perform this fitting step to retrieve those complex coefficients and hence could not retrieve the FR-LFPAD in Eq. (B10) (or, equivalently, the MF PAD). However, by retrieving the real coefficients $A_{JL}(k)$ we did retrieve the AR-LFPAD in Eq. (B11) where the θ -dependent is recovered, but the information about the laser polarization axis was lost from the integration over the azimuthal angle ϕ because of the cylindrically symmetric distribution. In terms of $A_{JL}(k)$, this AR-LFPAD can be rewritten as

$$\frac{d\sigma}{dkd\theta d\theta_k} = 2\pi \sum_{JL} A_{JL}(k) P_J(\cos \theta) P_L(\cos \theta_k), \quad (\text{B15})$$

which is the form that we use in this paper.

APPENDIX C: $A_{JL}(k)$ COEFFICIENTS FOR SELECTED CHANNELS

In this Appendix, we give in Tables I–III the $A_{JL}(k)$ coefficients for ionization channels presented in this paper. The coefficients are in arbitrary units; only their relative magnitudes are relevant.

- [1] D. Dill, Fixed-molecule photoelectron angular distributions, *J. Chem. Phys.* **65**, 1130 (1976).
- [2] D. M. Neumark, Time-resolved photoelectron spectroscopy of molecules and clusters, *Annu. Rev. Phys. Chem.* **52**, 255 (2001).
- [3] Y.-I. Suzuki, Direct relation of molecular orbital symmetry with photoelectron angular distributions from aligned molecules in the gas phase, *J. Phys. B* **41**, 215204 (2008).
- [4] T. Suzuki, Femtosecond time-resolved photoelectron imaging, *Annu. Rev. Phys. Chem.* **57**, 555 (2006).
- [5] Y. Arasaki, K. Takatsuka, K. Wang, and V. McKoy, Time-resolved photoelectron spectroscopy of wavepackets through a conical intersection in NO_2 , *J. Chem. Phys.* **132**, 124307 (2010).
- [6] F. Kelkensberg, A. Rouzée, W. Siu, G. Gademann, P. Johnsson, M. Lucchini, R. R. Lucchese, and M. J. J. Vrakking, XUV ionization of aligned molecules, *Phys. Rev. A* **84**, 051404(R) (2011).
- [7] G. R. Wu, P. Hockett, and A. Stolow, Time-resolved photoelectron spectroscopy: From wavepackets to observables, *Phys. Chem. Chem. Phys.* **13**, 18447 (2011).
- [8] A. Rouzée, A. G. Harvey, F. Kelkensberg, D. Brambila, W. K. Siu, G. Gademann, O. Smirnova, and M. J. J. Vrakking, Imaging the electronic structure of valence orbitals in the XUV ionization of aligned molecules, *J. Phys. B* **47**, 124017 (2014).
- [9] S. Minemoto, H. Shimada, K. Komatsu, W. Komatsubara, T. Majima, S. Miyake, T. Mizuno, S. Owada, H. Sakai, T. Togashi, M. Yabashi, P. Decleva, M. Stener, S. Tsuru, and A. Yagishita, Time-resolved photoelectron angular distributions from nonadiabatically aligned CO_2 molecules with SX-FEL at SACLA, *J. Phys. Commun.* **2**, 115015 (2018).
- [10] C. Marceau, V. Makhija, P. Peng, M. Hervé, P. B. Corkum, A. Y. Naumov, A. Stolow, and D. M. Villeneuve, Non-Born-Oppenheimer electronic wave packet in molecular nitrogen at 14 eV probed by time-resolved photoelectron spectroscopy, *Phys. Rev. A* **99**, 023426 (2019).
- [11] V. Kumarappan, L. Holmegaard, C. Martiny, C. B. Madsen, T. K. Kjeldsen, S. S. Viftrup, L. B. Madsen, and H. Stapelfeldt, Multiphoton Electron Angular Distributions from Laser-Aligned CS_2 Molecules, *Phys. Rev. Lett.* **100**, 093006 (2008).
- [12] C. Z. Bisgaard, O. J. Clarkin, G. Wu, A. M. D. Lee, O. Geßner, C. C. Hayden, and A. Stolow, Time-resolved molecular frame dynamics of fixed-in-space CS_2 molecules, *Science* **323**, 1464 (2009).

- [13] Y. Tang, Y.-I. Suzuki, T. Horio, and T. Suzuki, Molecular Frame Image Restoration and Partial Wave Analysis of Photoionization Dynamics of NO by Time-Energy Mapping of Photoelectron Angular Distribution, *Phys. Rev. Lett.* **104**, 073002 (2010).
- [14] P. Hockett, C. Z. Bisgaard, O. J. Clarkin, and A. Stolow, Time-resolved imaging of purely valence-electron dynamics during a chemical reaction, *Nat. Phys.* **7**, 612 (2011).
- [15] J. B. Williams, C. S. Trevisan, M. S. Schöffler, T. Jahnke, I. Bocharova, H. Kim, B. Ulrich, R. Wallauer, F. Sturm, T. N. Rescigno, A. Belkacem, R. Dörner, T. Weber, C. W. McCurdy, and A. L. Landers, Imaging Polyatomic Molecules in Three Dimensions Using Molecular Frame Photoelectron Angular Distributions, *Phys. Rev. Lett.* **108**, 233002 (2012).
- [16] H. Fukuzawa, S. Yamada, Y. Sakakibara, T. Tachibana, Y. Ito, T. Takanashi, T. Nishiyama, T. Sakai, K. Nagaya, N. Saito, M. Oura, M. Stener, P. Decleva, and K. Ueda, Probing gaseous molecular structure by molecular-frame photoelectron angular distributions, *J. Chem. Phys.* **151**, 104302 (2019).
- [17] H. Fukuzawa, R. R. Lucchese, X.-J. Liu, K. Sakai, H. Iwayama, K. Nagaya, K. Kreidi, M. S. Schöffler, J. R. Harries, Y. Tamenori, Y. Morishita, I. H. Suzuki, N. Saito, and K. Ueda, Probing molecular bond-length using molecular-frame photoelectron angular distributions, *J. Chem. Phys.* **150**, 174306 (2019).
- [18] V. Makhija, K. Veyrinas, A. E. Boguslavskiy, R. Forbes, I. Wilkinson, R. Lausten, S. P. Neville, S. T. Pratt, M. S. Schuurman, and A. Stolow, Ultrafast molecular frame electronic coherences from lab frame scattering anisotropies, *J. Phys. B* **53**, 114001 (2020).
- [19] J. Arlt, D. P. Singh, J. O. F. Thompson, A. S. Chatterley, P. Hockett, H. Stapelfeldt, and K. L. Reid, Photoelectron angular distributions from resonant two-photon ionisation of adiabatically aligned naphthalene and aniline molecules, *Mol. Phys.* **119**, e1836411 (2021).
- [20] J. G. Underwood and K. L. Reid, Time-resolved photoelectron angular distributions as a probe of intramolecular dynamics: Connecting the molecular frame and the laboratory frame, *J. Chem. Phys.* **113**, 1067 (2000).
- [21] T. Seideman, Time-resolved photoelectron angular distributions: Concepts, applications, and directions, *Annu. Rev. Phys. Chem.* **53**, 41 (2002).
- [22] Y.-I. Suzuki and T. Suzuki, Determination of ionization dynamical parameters by time-resolved photoelectron imaging, *Mol. Phys.* **105**, 1675 (2007).
- [23] A. Stolow and J. G. Underwood, Time-Resolved Photoelectron Spectroscopy of Nonadiabatic Dynamics in Polyatomic Molecules, *Advances in Chemical Physics*, Chap. 6 (John Wiley & Sons, Ltd, Hoboken, 2008), pp. 497–584.
- [24] S. Ramakrishna and T. Seideman, On the information content of time- and angle-resolved photoelectron spectroscopy, *J. Phys. B* **45**, 194012 (2012).
- [25] P. Hockett, General phenomenology of ionization from aligned molecular ensembles, *New J. Phys.* **17**, 023069 (2015).
- [26] C. Marceau, V. Makhija, D. Platzer, A. Y. Naumov, P. B. Corkum, A. Stolow, D. M. Villeneuve, and P. Hockett, Molecular Frame Reconstruction Using Time-Domain Photoionization Interferometry, *Phys. Rev. Lett.* **119**, 083401 (2017).
- [27] H. V. S. Lam, S. Yarlagadda, A. Venkatachalam, T. N. Wangjam, R. K. Kushawaha, C. Cheng, P. Svihra, A. Nomerotski, T. Weinacht, D. Rolles, and V. Kumarappan, Angle-dependent strong-field ionization and fragmentation of carbon dioxide measured using rotational wave packets, *Phys. Rev. A* **102**, 043119 (2020).
- [28] H. Hillenkamp, S. Keinan, and U. Even, Condensation limited cooling in supersonic expansions, *J. Chem. Phys.* **118**, 8699 (2003).
- [29] A. T. J. B. Eppink and D. H. Parker, Velocity map imaging of ions and electrons using electrostatic lenses: Application in photoelectron and photofragment ion imaging of molecular oxygen, *Rev. Sci. Instrum.* **68**, 3477 (1997).
- [30] F. Jin, H. Yang, H. Zhang, B. Wang, and W. Yang, Influence of polarization directions of the IR+XUV two-color laser fields on angle-resolved photoelectron energy spectrum, *Opt. Express* **29**, 10726 (2021).
- [31] V. Makhija, X. Ren, D. Gockel, A.-T. Le, and V. Kumarappan, Orientation resolution through rotational coherence spectroscopy, [arXiv:1611.06476](https://arxiv.org/abs/1611.06476).
- [32] X. Wang, A.-T. Le, Z. Zhou, H. Wei, and C. D. Lin, Theory of retrieving orientation-resolved molecular information using time-domain rotational coherence spectroscopy, *Phys. Rev. A* **96**, 023424 (2017).
- [33] P. Sándor, A. Sissay, F. Mauger, P. M. Abanador, T. T. Gorman, T. D. Scarborough, M. B. Gaarde, K. Lopata, K. J. Schafer, and R. R. Jones, Angle dependence of strong-field single and double ionization of carbonyl sulfide, *Phys. Rev. A* **98**, 043425 (2018).
- [34] P. Sándor, A. Sissay, F. Mauger, M. W. Gordon, T. T. Gorman, T. D. Scarborough, M. B. Gaarde, K. Lopata, K. J. Schafer, and R. R. Jones, Angle-dependent strong-field ionization of halomethanes, *J. Chem. Phys.* **151**, 194308 (2019).
- [35] H. Hu, S. Kangaparambi, M. Dörner-Kirchner, V. Hanus, A. Baltuška, M. Kitzler-Zeiler, and X. Xie, Quantitative retrieval of the angular dependence of laser-induced electron rescattering in molecules, *Phys. Rev. A* **103**, 013114 (2021).
- [36] G. A. Garcia, L. Nahon, and I. Powis, Two-dimensional charged particle image inversion using a polar basis function expansion, *Rev. Sci. Instrum.* **75**, 4989 (2004).
- [37] T. N. Wangjam, H. V. S. Lam, and V. Kumarappan, Strong-field ionization of the triplet ground state of O₂, *Phys. Rev. A* **104**, 043112 (2021).
- [38] R. N. Zare, *Angular Momentum: Understanding Spatial Aspects in Chemistry and Physics* (Wiley, New York, 1988), p. 121.
- [39] P. Hockett, M. Wollenhaupt, C. Lux, and T. Baumert, Complete Photoionization Experiments via Ultrafast Coherent Control with Polarization Multiplexing, *Phys. Rev. Lett.* **112**, 223001 (2014).
- [40] A. J. Yench, K. Ellis, and G. C. King, High-resolution threshold photoelectron and photoion spectroscopy of molecular nitrogen in the 15.0–52.7 eV photon energy range, *J. Electron Spectrosc. Relat. Phenom.* **195**, 160 (2014).
- [41] A. Ionin, S. Kudryashov, Y. Ponomarev, L. Seleznev, D. Sinitsyn, B. Tikhomirov, A. Tikhov, and V. Zvorykin, Absorption and ionization of molecular nitrogen by UV femtosecond laser pulses, *Opt. Commun.* **282**, 45 (2009).
- [42] A. V. Shutov, N. N. Ustinovskii, I. V. Smetanin, D. V. Mokrousova, S. A. Goncharov, S. V. Ryabchuk, E. S. Sunchugasheva, L. V. Seleznev, A. A. Ionin, and V. D. Zvorykin, Major pathway for multiphoton air ionization at 248 nm laser wavelength, *Appl. Phys. Lett.* **111**, 224104 (2017).

- [43] S. Petretti, A. Magaña, A. Saenz, and P. Decleva, Wavelength- and alignment-dependent photoionization of N_2 and O_2 , *Phys. Rev. A* **94**, 053411 (2016).
- [44] A. Lofthus and P. H. Krupenie, The spectrum of molecular nitrogen, *J. Phys. Chem. Ref. Data* **6**, 113 (1977).
- [45] W. C. Ermler, A. D. McLean, and R. S. Mulliken, Ab initio study of valence-state potential energy curves of nitrogen, *J. Phys. Chem.* **86**, 1305 (1982).
- [46] D. Pavičić, K. F. Lee, D. M. Rayner, P. B. Corkum, and D. M. Villeneuve, Direct Measurement of the Angular Dependence of Ionization for N_2 , O_2 , and CO_2 in Intense Laser Fields, *Phys. Rev. Lett.* **98**, 243001 (2007).
- [47] M. Wollenhaupt, M. Krug, J. Kohler, T. Bayer, C. Sarpe-Tudoran, and T. Baumert, Three-dimensional tomographic reconstruction of ultrashort free electron wave packets, *Appl. Phys. B* **95**, 647 (2009).
- [48] C. Smeenk, L. Arissian, A. Staudte, D. M. Villeneuve, and P. B. Corkum, Momentum space tomographic imaging of photoelectrons, *J. Phys. B* **42**, 185402 (2009).
- [49] J. Maurer, D. Dimitrovski, L. Christensen, L. B. Madsen, and H. Stapelfeldt, Molecular-Frame 3D Photoelectron Momentum Distributions by Tomographic Reconstruction, *Phys. Rev. Lett.* **109**, 123001 (2012).
- [50] C. Marceau, J. B. Bertrand, P. Peng, H. J. Wörner, P. B. Corkum, and D. M. Villeneuve, Simultaneous measurements of strong-field ionization and high harmonic generation in aligned molecules, *J. Phys. B* **53**, 084006 (2020).
- [51] M. Gregory, P. Hockett, A. Stolow, and V. Makhija, Towards molecular frame photoelectron angular distributions in polyatomic molecules from lab frame coherent rotational wavepacket evolution, *J. Phys. B* **54**, 145601 (2021).
- [52] D. M. Mintz and A. Kuppermann, Photoelectron spectroscopy of ethylene, isobutylene, trimethylethylene, and tetramethylethylene at variable angle, *J. Chem. Phys.* **71**, 3499 (1979).
- [53] X. M. Tong, Z. X. Zhao, and C. D. Lin, Theory of molecular tunneling ionization, *Phys. Rev. A* **66**, 033402 (2002).